

# The influence of geometric imperfections in cardiovascular FSI simulations



Lars Radtke\*, Marcel König, Alexander Düster

Hamburg University of Technology, Am Schwarzenberg-Campus 4c, 21073 Hamburg, Germany

## ARTICLE INFO

### Article history:

Available online 27 April 2017

### Keywords:

Cardiovascular fluid–structure interaction  
End-to-end anastomosis  
Soft tissue material  
Partitioned solution approach

## ABSTRACT

We present a study of the fluid–structure interaction in an idealized end-to-end anastomosis of a vascular bypass-graft and an artery. Special attention is paid to the impact of geometric imperfections in the artery and the flow path of the upstream vessel segment on the hemodynamics. A partitioned solution approach is applied and developed further to solve the coupled problem in an implicit manner. To stabilize and accelerate the convergence of the staggered coupling iterations, an interface quasi-Newton least squares method is applied. While the finite volume method is used for the fluid mechanics subproblem, high-order finite elements serve to discretize the structural subproblem. A convergence study shows the efficiency of the high-order elements in the context of nearly incompressible, anisotropic materials used to model circular and irregular-shaped segments of an artery. The fluid–structure interaction simulations reveal a dominant influence of the upstream vessel's curvature, which, however, decays rapidly in straight sections where the influence of geometric imperfections is dominant. Based on the proposed simulation approach, hemodynamic parameters such as the oscillating shear index can be directly linked to the shape and the intensity of the imperfections.

© 2017 Elsevier Ltd. All rights reserved.

## 1. Introduction

Cardiovascular fluid–structure interaction (FSI), i.e. the interaction of pulsating blood flow and deformable vessels, has been addressed numerically from many different perspectives and on many different scales. Early examples include the investigation of pulse wave propagation through the arterial system as a whole using reduced-order models, see e.g. [1,2]. The development of computational methods for general structural and fluid dynamics problems now allows for an in-depth investigation of local hemodynamic phenomena using highly sophisticated simulation techniques. If the interaction of the structure and fluid is modeled using a simplified description, three-dimensional simulations that cover large parts of the vascular system can be performed in acceptable time [3]. Fully coupled approaches are restricted to smaller segments of the cardiovascular system, but they have nonetheless been used for successful investigations of the hemodynamics, e.g. in aneurysms [4–6] or stenoses [7]. Clinical applications for such investigations range from surgical planning for a specific patient to more general purposes such as investigating the hemodynamics in vessels shaped according to certain characteristics [8]. Local hemodynamic factors such as the wall shear stress (WSS) and related quantities as well as structural quantities like the stress in the vessel wall have been found to promote the development of cardiovascular diseases, see e.g. [9] for a more detailed discussion. The methods, which were developed in the scope of the cited references, allow to predict these factors and they serve as a valuable tool in the optimization of surgical techniques or vascular substitutes.

\* Corresponding author.

E-mail address: [lars.radtke@tuhh.de](mailto:lars.radtke@tuhh.de) (L. Radtke).

Here, we focus on the influence of geometric imperfections in the vessel wall on the hemodynamics. With the simulation approach presented in [10], we investigate the FSI regarding the connection between a vascular bypass graft and an artery (end-to-end anastomosis). The geometry of the artery is distorted in a smooth way, leading to different models that are considered in the analysis. This allows to correlate geometric features such as dips and hemodynamic factors like the WSS as already proposed in [11]. In the present work, we follow this idea in a more detailed way using state-of-the-art soft tissue material models and partitioned coupling schemes. We further pay special attention to the structural mechanics subproblem, which we solve using high-order finite elements. A convergence study is performed for regular and irregular shaped vessels to show the efficiency of the method.

**Fluid–structure interaction.** The rapid development of different solution approaches to FSI problems, see e.g. [12–14], offers the possibility to perform relevant studies in the context of numerous applications including cardiovascular studies. Regardless of the application, such problems can be seen as surface-coupled multifield problems, where the computational domain is divided into two parts, one representing the structure and the other representing the fluid. Torii et al. [15,16,6] were among the first to address the simulation of the FSI in arteries using such general solution approaches. Since then, the methods have been customized and refined by many more researchers [17–21]. From a physical point of view, a similar phenomenon is investigated in the cited studies: the pulsatile flow of a viscous, possibly non-Newtonian fluid through a segment of a network of elastic pipes (arteries). However, a variety of different solution approaches to the FSI-problem and discretization methods for the structural and fluid mechanics subproblems are employed. While in [17–21] the FSI problem is solved monolithically, i.e. the subproblems are solved simultaneously using one discretization method, a partitioned solution approach is followed in [22,23]. This allows to employ different discretization methods for the structural and fluid mechanics subproblem. While partitioned approaches may introduce stability problems, especially in cardiovascular FSI studies [24], it was shown in [10] that they can be overcome using sophisticated coupling strategies like the quasi-Newton methods proposed and investigated in [25–29]. To this end, we employ the modified version of the interface quasi-Newton least squares (IQNLS) method [10] to accelerate and stabilize the coupling iterations. In simulations of the mentioned phenomenon, this approach has been shown to stabilize the coupling iterations also for problems with little or no structural damping.

**Structural modeling.** The material behavior of soft tissues is characterized by their micro-mechanic structure. In arteries, the two helically wound families of collagen fibers lead to a transversely isotropic behavior with two preferred directions which are mirrored in the axial direction. A widely employed model that accounts for this histology is the Holzapfel–Gasser–Ogden (HGO) material model proposed in [30]. It is suitable to describe the response of an artery starting from an unloaded state up to physiological pressures and has been further developed in many works, see [31–33] and the references cited therein. However, in FSI simulations it is common to use simplified material models, which overestimate the stiffness in low pressure ranges, see e.g. [15,5,4,22,23]. This is a reasonable choice if one is only interested in higher pressure ranges (most commonly the typical range 80–120 mmHg), but this approach is not suitable for modeling connections to vascular substitutes that are established in the unloaded state.

In [10] it was shown that the HGO model can be applied successfully in the context of partitioned cardiovascular FSI simulations. While the large deformations according to the low stiffness at low pressure ranges introduced stability issues when using conventional relaxation schemes, they could be overcome with the modified IQNLS method. We employ the  $p$ -version of the finite element method ( $p$ -FEM) as described in [34] to discretize the structural mechanics subproblem. It is known to overcome locking problems introduced by nearly incompressible, anisotropic materials or thin-walled structures. As the typical structural subproblem in cardiovascular FSI simulations has all of these characteristics, we choose the  $p$ -FEM as the preferred discretization method.

**Outline.** The remainder of this work is structured as follows: In the next section we give a brief explanation of the partitioned solution approach including the underlying equations of the fluid and the structural mechanics subproblem. Further, the properties of the chosen variant of the high-order finite element method are summarized here. In Section 3, we give details regarding the numerical studies, i.e. a convergence study of the structural mechanics subproblem and the FSI simulation. The corresponding results are presented Section 4, and a conclusion is drawn in Section 5.

## 2. Partitioned fluid–structure interaction

A *partitioned solution approach* here denotes the complete separation of the involved subproblems. Each of them may be solved using a different discretization strategy and practically a different software, we denote here as *field solver*. The field solvers are steered by a coupling software which treats them as black boxes, able to get a certain input, give a certain output and – as far as dynamic simulations are considered – can march forward in time, see Fig. 1. We use the coupling software *comana*, which allows for a flexible *remote control-like* steering of a variety of field solvers. A detailed overview on coupled problems and the software *comana* can be found in [35].

In a fluid–structure interaction problem, there are two subproblems, the well-known initial boundary value problems (IBVP) from fluid and structural dynamics. A structural solver approximates the dynamic state of a structure and receives as input tractions at the Neumann boundaries of the underlying IBVP. It marches forward in time according to the given tractions, delivering displacements as output. While this is a standard procedure also in uncoupled simulations, a slight change has to be made to the solver to ensure that it can be used in a coupled simulation as sketched in Fig. 1. It has to offer the possibility to go back in time and to redo one or possibly more time steps, according to different tractions. If a fluid solver

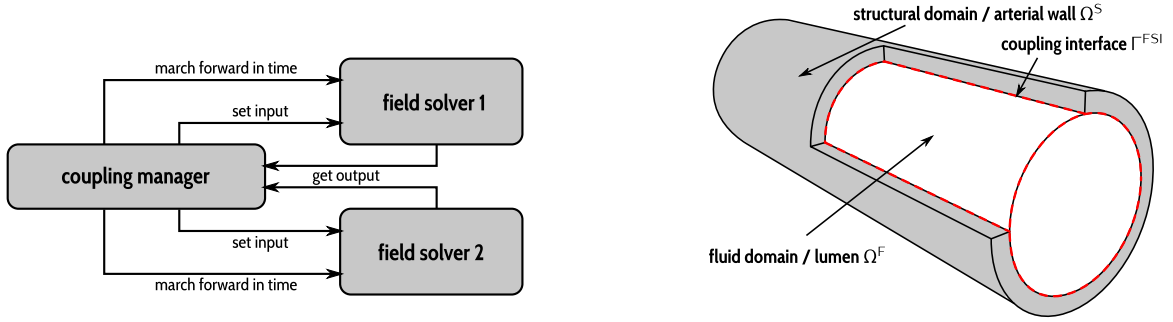


**Fig. 1.** Left: Software interaction—A coupling manager *remote controls* the field solvers involved in the solution of the multifield problem. Right: Split of the computational domain in a partitioned cardiovascular FSI simulation.

is coupled in a similar way, but providing traction as output and taking displacements as input, a fully coupled partitioned FSI simulation can be established. Fig. 1 shows a corresponding separation of the computational domain into a fluid mechanics part  $\Omega^F$  and a structural mechanics part  $\Omega^S$  sharing the boundary  $\Gamma^{FSI}$ , correspondingly called *coupling interface* or *wet surface*. In the following, the basic equations of the fluid and structural mechanics subproblems are summarized, followed by the coupling procedure used in this study.

### 2.1. Structural dynamics

As described in many standard textbooks such as [36–38,34,39], the motion and deformation of an elastic body may be described by the balance of linear momentum

$$\rho_0 \ddot{\mathbf{d}} + \text{DIV}(\mathbf{FS}) + \rho_0 \mathbf{b} = \mathbf{0} \quad \text{in } \Omega_0^S \quad (1)$$

augmented by Neumann and Dirichlet boundary conditions

$$\mathbf{S} \mathbf{N} - \bar{\mathbf{t}} = \mathbf{0} \quad \text{on } \Gamma_0^{ts} \subset \partial \Omega_0^S, \quad (2)$$

$$\mathbf{d} - \bar{\mathbf{d}} = \mathbf{0} \quad \text{on } \Gamma_0^{ds} \subset \partial \Omega_0^S, \quad (3)$$

and appropriate initial conditions. Here,  $\rho$  denotes the body's density,  $\mathbf{b}$  is a force per unit mass,  $\mathbf{N}$  is the unit outward normal of  $\Gamma_0^{ts}$  and  $\bar{\mathbf{t}}$  and  $\bar{\mathbf{d}}$  are prescribed traction and displacement boundary values, respectively. The deformation gradient and the second Piola–Kirchhoff stress tensor are denoted by  $\mathbf{F}$  and  $\mathbf{S}$ , respectively. Quantities marked with the subscript  $(\cdot)_0$  as well as the divergence operator  $\text{DIV}(\cdot)$  are to be understood with respect to an *undeformed and stress-free reference configuration* at time  $t = 0$ . Prestrains, which usually are present in arteries, see e.g. [30,40], are neglected.

To solve the IBVP (1)–(3), we need a constitutive relation that relates deformations, i.e. strains, and stresses. Restricting ourselves to hyperelastic materials, a corresponding constitutive model is defined by a strain energy density function (SEDF). In this work, the Neo-Hookean SEDF

$$W^{\text{NH}} = \frac{1}{2} \mu (\text{I}_{\mathbf{C}} - 3) - \mu \ln(J) + \frac{\kappa}{2} \ln(J)^2, \quad (4)$$

see e.g. [37], as well as the Holzapfel–Gasser–Ogden (HGO) SEDF

$$W^{\text{HGO}} = \frac{k_1}{2k_2} \left( e^{k_2(\text{IV}_{\mathbf{C}}-1)^2} + e^{k_2(\text{VI}_{\mathbf{C}}-1)^2} - 2 \right) + \frac{\mu}{2} \left( J^{-\frac{2}{3}} \text{I}_{\mathbf{C}} - 3 \right) + \frac{\kappa}{2} (J - 1)^2 \quad (5)$$

see e.g. [30,33,32] are used. Therein,  $\text{I}_{\mathbf{C}} = \text{tr}(\mathbf{C})$ ,  $\text{II}_{\mathbf{C}} = \text{tr}(\mathbf{C}^2)$  denote the first and second invariants of the right Cauchy–Green deformation tensor. For the other two invariants  $\text{IV}_{\mathbf{C}} = \mathbf{a}_1 \cdot \mathbf{C} \mathbf{a}_1$  and  $\text{VI}_{\mathbf{C}} = \mathbf{a}_2 \cdot \mathbf{C} \mathbf{a}_2$  hold, where  $\mathbf{a}_i$  is the local fiber direction of the fiber family  $i$ .  $J$  denotes the determinant of the deformation gradient,  $\mu$ ,  $\kappa$ ,  $k_1$  and  $k_2$  are material parameters. As can be seen, all SEDFs are used in their compressible variant. The HGO model was first introduced as an incompressible model in [30]. While in [33] a compressible variant is introduced with all terms involving only the isochoric right Cauchy–Green tensor  $\bar{\mathbf{C}} = J^{-\frac{2}{3}} \mathbf{C}$ , we follow the remark from [32] and use the invariants of  $\mathbf{C}$  rather than those of  $\bar{\mathbf{C}}$  in the anisotropic terms related to the stiffness of the fibers. For detailed information on hyperelastic material models and their implementation in a finite element context we refer the reader to [41]. The initial boundary value problem (1)–(3) is solved in its weak form using the  $p$ -version of the finite-element method as explained in Section 2.4. The Newmark- $\beta$  method is used to discretize the resulting system of ordinary differential equation in time. While the Newmark parameters are set in such a way that no numerical damping is introduced, mass proportional damping with a factor of  $\alpha = 0.01$  is added. As shown in [10], this will stabilize and accelerate the convergence of the coupling iterations while changing the results only to a negligible extent. Furthermore, a nonzero damping matrix can be justified by the damping effects of the surrounding tissue, see, for

example, [42]. However, based on the results from [10] we expect to get results which are very close to what we would get for  $a = 0$ . Summarizing, the results in the present work correspond to the nearly undamped case, while in [10] a focus lies on investigating the influence of damping on the results and on the performance of the partitioned solution strategy.

## 2.2. Fluid dynamics

The dynamics of an incompressible viscous fluid are described by the incompressible Navier–Stokes equations

$$\operatorname{div} \mathbf{u} = 0 \quad (6)$$

$$\dot{\mathbf{u}} + (\mathbf{u} - \mathbf{u}^M) \operatorname{grad} \mathbf{u} + \operatorname{div}(\nu \operatorname{grad} \mathbf{u}) + \varrho^{-1} \operatorname{grad} p = \mathbf{0} \quad (7)$$

which hold in  $\Omega^F$ , see e.g. [43–45]. Again,  $\varrho$  denotes the density,  $\nu$  is the dynamic viscosity. The fluid's state is defined by the velocity  $\mathbf{u}$ , acceleration  $\dot{\mathbf{u}}$  and pressure  $p$ . As flow in a moving domain is considered, the mesh velocity field is included in the equation by  $\mathbf{u}^M$ . In this work, the following pressure and velocity boundary conditions are considered:

$$p - \bar{p} = 0 \quad \text{and} \quad \mathbf{u} \cdot \mathbf{n} = 0 \quad \text{on} \quad \Gamma^p \subset \partial\Omega^F \quad (8)$$

$$\mathbf{u} - \bar{\mathbf{u}} = \mathbf{0} \quad \text{and} \quad \operatorname{grad} p \cdot \mathbf{n} = 0 \quad \text{on} \quad \Gamma^u \subset \partial\Omega^F \quad (9)$$

where  $\mathbf{n}$  denotes the unit outward normal of the fluid domain  $\Omega^F$  and  $\bar{p}$  and  $\bar{\mathbf{u}}$  are prescribed boundary values. As typical fluid dynamic quantities, which have been identified with the development of cardiovascular diseases, we evaluate the wall shear stress  $\boldsymbol{\tau}_w = \varrho \nu \operatorname{symgrad}(\mathbf{u})\mathbf{n}$  and the oscillating shear index (OSI)

$$\text{OSI} = \frac{1}{2} \left( 1 - \frac{\left\| \int_t^{t+T} \boldsymbol{\tau}_w \, dt \right\|_2}{\int_t^{t+T} \|\boldsymbol{\tau}_w\|_2 \, dt} \right). \quad (10)$$

With the period or duration of one beat of the heart  $T$ , the OSI provides an average measure for the changes in direction of the WSS  $\boldsymbol{\tau}_w$ .

The initial boundary value problem (6)–(9) is solved using the finite-volume method. We apply the solver *pimpleDyM-Foam* from the software package *OpenFOAM* [46,47]. It implements an implicit variant of the PISO (Pressure Implicit with Split of Operators) algorithm, including an implicit Euler scheme for time integration. In [35] the solver was successfully used in combination with the coupling manager *comana* to solve several benchmark cases. It can effectively handle large mesh deformations, i.e. no remeshing is needed, see also [48,10].

## 2.3. Coupling scheme

With the formulations of the fluid and the structural mechanics subproblems at hand, the coupling conditions can be stated:

1. equality of interface kinematics:  $\bar{\mathbf{d}}^M = \mathbf{d}$  and  $\bar{\mathbf{u}} = \mathbf{u}^M$
2. equality of interface tractions:  $\bar{\mathbf{t}} = p\mathbf{n} + \boldsymbol{\tau}_w$ .

Here,  $\bar{\mathbf{d}}^M$  denotes the displacement of the fluid mesh. The mesh velocity  $\mathbf{u}^M$  is calculated within the fluid solver such that  $\mathbf{u}^M = \dot{\mathbf{d}}^M$ . The conditions must hold on the coupling interface  $\Gamma^{\text{FSI}} = \partial\Omega^F \cap \partial\Omega^S$ . As can be seen,  $\Gamma^{\text{FSI}} \subset \Gamma^t$  within the structural mechanics subproblem and  $\Gamma^{\text{FSI}} \subset \Gamma^u$  within the fluid mechanics sub-problem.

If a structural solver step – i.e. the calculation of interface displacements according to interface tractions for time step  $i$  – is denoted by  $\mathbf{d}_i^{\Gamma^{\text{FSI}}} = \mathcal{S}(\mathbf{t}_i^{\Gamma^{\text{FSI}}})$  and, correspondingly, a fluid solver step is denoted by  $\mathbf{t}_i^{\Gamma^{\text{FSI}}} = \mathcal{F}(\mathbf{d}_i^{\Gamma^{\text{FSI}}})$ , the coupled FSI problem can be stated as a fixed-point equation

$$\mathbf{d}_i^{\Gamma^{\text{FSI}}} = \mathcal{S} \circ \mathcal{F}(\mathbf{d}_i^{\Gamma^{\text{FSI}}}). \quad (11)$$

If solved with a fixed-point iteration (FPI), the solution process within every time step can be stated as

$$\mathbf{d}_{i,k+1}^{\Gamma^{\text{FSI}}} \stackrel{\text{FPI}}{=} \mathcal{S} \circ \mathcal{F}(\mathbf{d}_{i,k}^{\Gamma^{\text{FSI}}}). \quad (12)$$

However, in the context of FSI, such a fixed-point iteration is prone to instabilities and will converge only for very simple problems. Therefore, convergence acceleration methods have to be applied, which, from the sequence of displacements calculated from the structural solver, compute an improved update  $\mathbf{d}_{k+1}^{\Gamma^{\text{FSI}}}$ . Within this process, such algorithms work with the discretized displacement at the interface  $\mathbf{d}_{k+1}^{\Gamma}$  (upright letter). The mesh motion solver, which is part the FVM fluid solver, expects as input this displacement at the nodes of the underlying mesh. At the same time, the FEM structural solver expects as input tractions at the quadrature points of the finite element's boundaries. Therefore, denoting the convergence

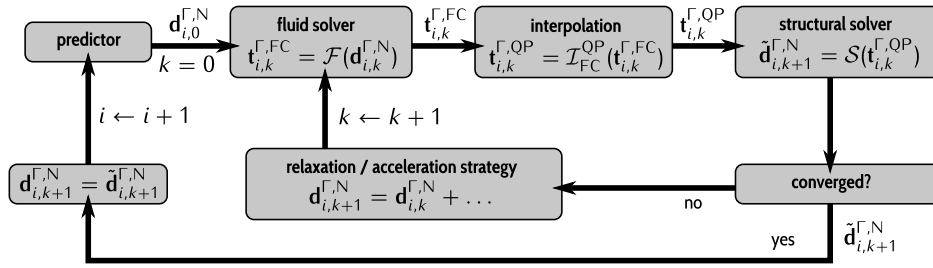


**Fig. 2.** Solution procedure followed in each time step of the coupled FSI simulation.  
Source: Taken from [10].

acceleration step by  $\mathcal{A}$  and an interpolation step from a point cloud  $A$  to a point cloud  $B$  by  $\mathcal{I}_A^B$ , the coupling iteration in terms of the discretized quantities reads

$$\mathbf{d}_{i,k+1}^{\Gamma,N} = \mathcal{A} \circ \mathcal{I}_M^N \circ \mathcal{S} \circ \mathcal{I}_{FC}^{QP} \circ \mathcal{F}(\mathbf{d}_{i,k}^{\Gamma,N}). \quad (13)$$

Here, FC, N, M, and QP denote the fluid mesh's face centers, the fluid mesh's nodes, the structural mesh's nodes and the structural mesh's quadrature points. The solution process followed in every time step is also depicted in Fig. 2. The interpolation operator  $\mathcal{I}_M^{FC}$  does not appear as a separate block since the interpolation is performed within the structural solver using the shape functions of the finite elements.

We use the modified version of the interface quasi-Newton least squares method as introduced in [10] to accelerate the fixed-point iteration. It has shown to work well also in the case of cardiovascular FSI simulations with little or no structural damping and soft tissue material. The fixed-point iteration is performed until one of the following convergence criteria is fulfilled:

$$\frac{\|\mathbf{d}_{i,k+1}^{\Gamma,N} - \mathbf{d}_{i,k}^{\Gamma,N}\|}{\|\mathbf{d}_{i,k}^{\Gamma,N}\|} < e_{\text{rel}}, \quad \|\mathbf{d}_{i,k+1}^{\Gamma,N} - \mathbf{d}_{i,k}^{\Gamma,N}\| < e_{\text{abs}}. \quad (14)$$

## 2.4. High-order finite element method

The  $p$ -FEM was originally introduced in [49] and has since been applied in many fields of computational mechanics. It has been shown to overcome locking problems faced in low-order pure displacement-based formulations. Locking is characterized by a severe underestimation of the displacements and typically occurs if nearly incompressible or anisotropic materials or thin-walled structures are considered [50–52]. While mixed formulations may circumvent the problem of locking, other issues like numerical instabilities and the need for special formulations of constitutive models may be introduced by such element types. Opposed to that, high-order finite elements as well as other high-order methods like isogeometric analysis [53] provide an elegant method that can overcome all locking phenomena without deviating from the typical displacement formulation usually applied in structural mechanics problems. In the context of structural mechanics simulations of soft tissues, higher-order methods are especially attractive due to the characteristics of such structures. They are in general thin-walled and show an anisotropic nearly incompressible material behavior [30]. We thus choose the  $p$ -FEM as the preferred discretization method for the structural mechanics sub-problem of the FSI analysis. It is augmented by the quasi-regional mapping technique proposed in [54] and, like in [55,56], anisotropic ansatz spaces are used. To this end, we use integrated Legendre polynomials to form a hierarchic basis of shape functions that span the space of polynomials up to a certain degree  $p$ . Tensor product spaces and trunk spaces are used, possibly with a different polynomial degree  $p_T$  in the thickness direction of the structure. A detailed description of the spaces is provided in [34,55]. The quasi-regional mapping technique serves to represent curved element faces and edges using a polynomial description. The real geometry is interpolated by the basis functions (Lagrange polynomials) from another space with maximum degree  $p_G$ , which, in this case, is chosen to be a serendipity-type space, including polynomials up to order  $p_G$  along the edges only. While the standard quasi-regional mapping technique includes such higher modes also along the element's faces, using *edge-blending* only ensures an iso- or subparametric element formulation also for trunk spaces as long as  $p \geq p_G$ . This is favorable with regard to artificial strains which may be introduced by a superparametric element formulation in the context of large rigid body rotations.

## 3. Numerical investigations

To find the best combination of element size and polynomial degree of the shape functions, we consider several test cases. To this end, it is possible to freely choose the polynomial degree of the shape functions in three local element directions, the polynomial degree used for the geometry (mapping) as well as the element size. The convergence of the strain energy, the displacement, and the von Mises stress are investigated for different choices of these parameters. In consideration of the

**Table 1**  
Material parameters for bypass-graft (Neo-Hooke) and artery (HGO).

	HGO (media)	HGO (adventitia)	Neo-Hooke
Shear modulus $\mu$ in N/m <sup>2</sup>	$5.4 \times 10^4$	$5.4 \times 10^3$	$3.33 \times 10^5$
Bulk modulus $\kappa$ in N/m <sup>2</sup>	$1.0 \times 10^9$	$1.0 \times 10^8$	$1.67 \times 10^9$
Fiber angle $\beta$ in °	10.0	40.0	
Fiber stiffness $k_1$	$0.64 \times 10^3$	$5.1 \times 10^3$	
Fiber stiffness $k_2$	3.54	15.4	

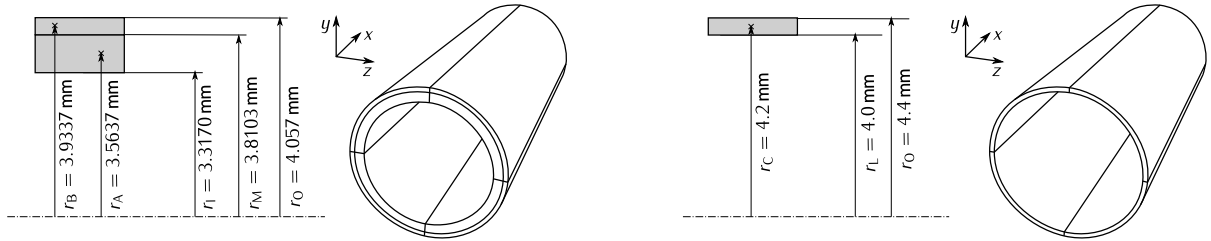


**Fig. 3.** Initial mesh for test cases *circular shaped artery* (left) and *idealized bypass-graft* (right).

results of this convergence study, a reasonable discretization is chosen for the FSI problem. In all simulations, the material parameters are set according to Table 1.

### 3.1. Test cases

All test cases consist of a tube, which is loaded with an internal pressure of  $p_{\text{internal}} = 1.6 \times 10^4 \text{ Pa} \approx 120 \text{ mmHg}$ . Starting from the undeformed, stress free reference configuration, the pressure is increased over 10–20 load steps, such that the Newton–Raphson method applied to solve the discretized non-linear equilibrium equations converges properly. A plane strain situation is induced by preventing a displacement in  $x$ -direction at the ring-shaped ends of all models. In the symmetric test cases, the displacement of nodes in the  $x$ - $y$  and the  $x$ - $z$  plane is prevented accordingly to avoid rigid body movements. In the non-symmetric test cases, only two nodes on one end of the model are prevented from moving in  $x$  or  $y$  direction, respectively, for the same purpose. For comparability reasons, all geometries are fully discretized without further exploiting any symmetries. The following relative error measures are considered in the convergence studies:

$$e_E = \frac{E - E^{\text{ref}}}{E^{\text{ref}}}, \quad e_d = \frac{\|\mathbf{d}^{\text{ref}} - \mathbf{d}\|}{\|\mathbf{d}^{\text{ref}}\|}, \quad e_{\sigma_v} = \frac{\|\sigma_v^{\text{ref}} - \sigma_v\|}{\|\sigma_v^{\text{ref}}\|}. \quad (15)$$

Therein,  $E$  denotes the strain energy,  $\mathbf{d}$  and  $\sigma_v$  denote vectors collecting the displacement and von Mises stress at  $n$  evaluation points, such that

$$\mathbf{d} = [\mathbf{d}^T(\mathbf{X}_1) \dots \mathbf{d}^T(\mathbf{X}_n)]^T \quad \text{and} \quad \boldsymbol{\sigma} = [\sigma_v(\mathbf{X}_1) \dots \sigma_v(\mathbf{X}_n)]^T. \quad (16)$$

If not stated otherwise, the  $n$  evaluation points are taken to be the finite element's centers and reference solutions are obtained using a discretization with a polynomial degree of  $p^{\text{ref}} = 10$ .

1. *Circular shaped artery.* The first test case is depicted on the left-hand side of Fig. 3. The circular model of the segment of an artery with the dimensions taken from [32] consists of two layers, according to the original formulation of the HGO material model in [30]. They mimic the artery's layers *media* and *adventitia*, while the much thinner inner layer *intima* is neglected. The material properties for the HGO model, as given in Table 1 were determined in [57].

2. *Idealized bypass-graft.* The thin-walled tube depicted on the right-hand side of Fig. 3 is the subject of the second test case. Here, the Neo-Hooke model is applied, with parameters as given in Table 1. With these specifications, the model roughly represents an idealized bypass-graft made from PTFE with an almost linear relationship between internal pressure and change in diameter, as reported in [58].

3. *Irregular shaped artery.* We further consider an irregular shaped segment of an artery, which is randomly distorted in a smooth way. Starting with the geometry of the first test case, a smooth bicubic spline  $d$  is used to alter the radius locally. Considering the radius as a function of the global  $x$ -direction and the circumferential coordinate  $\varphi$  it is given by

$$r(x, \varphi) = \begin{cases} r_L - d(x, \varphi) & \text{for the lumen,} \\ r_M - \frac{1}{3} d(x, \varphi) & \text{for the media,} \\ r_A & \text{for the adventitia.} \end{cases} \quad (17)$$



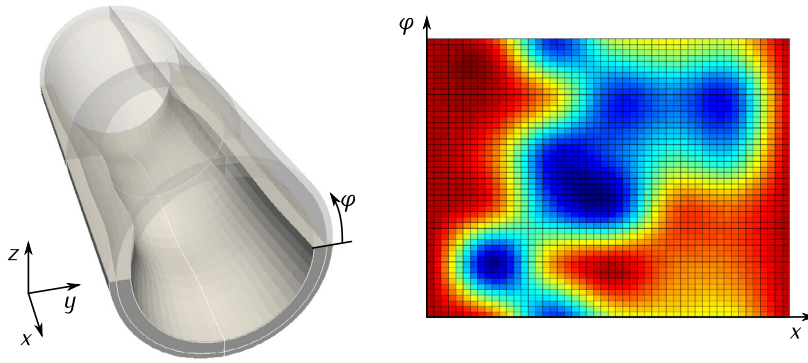


Fig. 4. Initial mesh for test case *irregular shaped artery* (left) and corresponding radius deviation  $d$  (right).

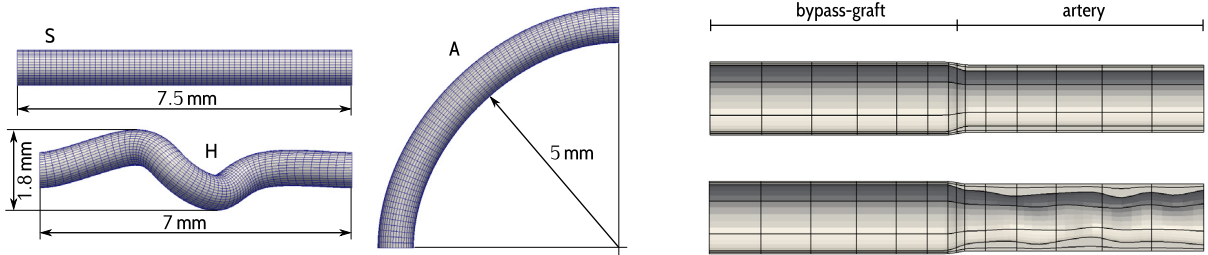


Fig. 5. Fluid meshes for the rigid extensions of the FSI domain (left) and cut through the smooth ( $d^{\max} = 0$  mm) and most deformed ( $d^{\max} = 0.75$  mm) structural mesh (right).

With  $0 \text{ mm} \leq d(x, \varphi) \leq 1 \text{ mm}$ , this mimics a thickening of the vessel wall towards the inside, while the outer radius of the adventitia layer remains unchanged. The resulting mesh and the radius deviation  $d(x, \varphi)$  constructed using a bicubic spline with 7 and 5 support points in the  $x$ - and  $\varphi$ -directions, respectively, are given in Fig. 4. As can be seen, control points with  $x = 0$  and  $x = x_{\max}$  are set to zero to preserve a regular shape at the ends of the model.

### 3.2. FSI study

According to the results of the convergence study presented in Section 4, we discretize an idealized end-to-end connection of a bypass graft and an artery (end-to-end anastomosis). As our goal is to study the influences of geometry imperfections in the vessel wall on the hemodynamics, different variants of the anastomosis are modeled. Fig. 5 shows two of the models considered here. They are created starting from the circular shaped model and introducing an imperfection by means of the same technique that was used to create the irregular shaped model of the third test case *irregular shaped artery*. Like the material parameters the dimensions of bypass graft and artery in the thickness direction are taken to be the same as in the test cases. A smooth transition between the two cross sections is obtained by blending them into each other using cosine functions. In total, four models are created using the same spline surface, but scaling it in such a way that the maximum radius deviation  $d^{\max}$  is 0, 0.25, 0.5 or 0.75 mm, respectively.

As shown in Fig. 5, we further consider different paths for the upstream part of the bypass-graft. These are modeled as rigid, i.e. no FSI is considered in this section. In the straight case (S), this *rigid extrusion* of the inlet of the fluid domain ensures a proper pulsating velocity profile at the inlet of the FSI section even if non-Womersley-type velocity profiles are prescribed on the boundary. In the helical (H) and arc-shaped (A) case, the rigid extrusion leads to completely different velocity profiles at the inlet of the FSI section. This provides a reference for the study of the influence of the geometry imperfections. While the studies in [11] already indicated that the shape of the upstream vessel path has a much larger influence on WSS-related quantities than geometry imperfections, we would like to investigate this in more detail here. Fig. 6 shows one of the 12 models resulting from a combination of the different rigid extensions and anastomosis models. For each model, we carry out a partitioned FSI simulation according to the procedure summarized in Section 2. Each simulation covers three beats of the heart, a first one to drive the model to the state of physiological pressure and flow ranges, a second one to investigate the quantities of interest and a third one to ensure periodicity. A flow as given in Fig. 6 is prescribed at the inlet of the fluid domain. At the outlet, the pressure is prescribed according to a two-element windkessel model. The scaling procedure from [10] and the parameters given therein are used to arrive at the pressure range of interest ( $\approx 80$ –120 mmHg). The structural model is clamped at both ends. Throughout the simulation, a time step size of  $\Delta t = 0.002$  s is maintained.

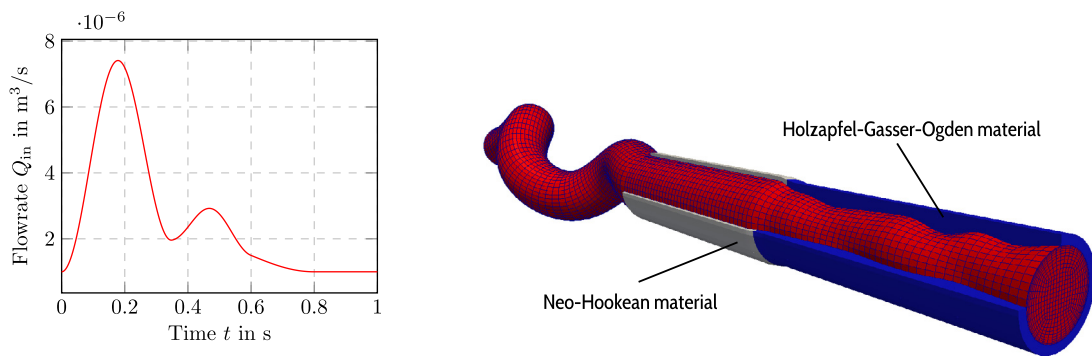


**Fig. 6.** Left: Flow rate  $Q_{in}$  prescribed at the fluid domain's inlet. Right: Complete FSI model with fluid mesh (red) and structural meshes for bypass section (gray) and artery section (blue). (For interpretation of the references to color in this figure legend, the reader is referred to the web version of this article.)

## 4. Results

In this section, we analyze the results starting with the convergence study of the structural subproblem. The mesh for the FSI study presented in Section 3 is based on these results. The second part of this section serves to present the results of the FSI study.

### 4.1. Convergence study

We start with the test case *circular shaped artery* as depicted in Fig. 3. In Fig. 7, the relative error in strain energy is plotted for different discretizations. The first thing to notice here is that the trunk space shows a much higher efficiency compared to the tensor product space, i.e. less degrees of freedom are needed to achieve the same accuracy. Further, an isotropic mesh refinement cannot improve the efficiency. While a superior convergence rate of the trunk space compared to the tensor product space was already observed in [55] as well as in [32] (for circular shaped arteries described with the HGO material model), Fig. 7 additionally shows the performance of anisotropic ansatz spaces. As can be seen, fixing the ansatz order in the thickness direction  $p_T$  leads to an improved convergence for the tensor product space. Here,  $p_T = 3$  is sufficient to obtain a fairly small error (from an engineering point of view) of  $e_E < 10^{-4}$ . However, as expected for a fixed ansatz order in one direction, the error cannot be reduced beyond a certain limit. Finally, the results from Fig. 7 show that a similar behavior is obtained using anisotropic variants of the trunk space but that they do not increase the efficiency. The trunk space further shows an unexpectedly low error for all computations with  $p_T = 3$ , which leads to a non-monotonic convergence for the standard setting. However, monotonic convergence is restored, if the order of the quadrature  $p_I$  is increased, see Fig. 7. For the circular shaped artery, we thus find the isotropic trunk space to lead to the most efficient discretization. Fig. 8 shows that this statement holds also for the convergence of displacements and stresses—using the trunk space in combination with the initial mesh leads to the most efficient discretization. As shown for the strain energy, the anisotropic variants of the trunk space do not lead to an improved convergence either, and they were left out in Fig. 8 for clarity. Continuing with the second test case *idealized bypass graft*, which is characterized by a much lower wall thickness and a Neo-Hookean material model instead of the HGO material model, we also find that the trunk space is more efficient than the tensor product space, see Fig. 9. Again, neither a mesh refinement nor a fixed polynomial degree in thickness direction improves the convergence.

The results obtained for the test case *irregular shaped artery* are summarized in Fig. 10. Here, a mesh refinement is needed to accurately represent the geometry with the chosen setting for the quasi-regional mapping, where we apply mapping functions of the same polynomial degree as the shape functions used to discretize the displacement field. It can be observed that for the initial mesh, the geometry error is dominant and that it prevents the solution from converging properly. As in the previous cases, the isotropic trunk space leads to the most efficient discretization.

Concluding, it can be said that the high convergence rate expected from the  $p$ -FEM for smooth problems can be realized for the typical structural problem arising in cardiovascular mechanics. Neither the nearly incompressible thin-walled structure of the bypass graft nor the anisotropic material model leads to locking problems of any kind, as long as the mesh size and the polynomial degree of the shape functions are selected carefully. For the first time, this was also shown for an irregular shaped segment of an artery. At the same time, the convergence study revealed that for the present test cases, a reduction of the polynomial degree in thickness direction is not advisable—at least not for the favored trunk space. This in turn shows that these problems are of true three-dimensional nature, which makes the use of structural elements, i.e. shells, questionable.

### 4.2. FSI study

According to Section 3, we simulate the FSI in twelve variants of an idealized end-to-end anastomosis. To get an impression of the general course of these FSI simulations, selected global quantities are plotted against time in Fig. 11.



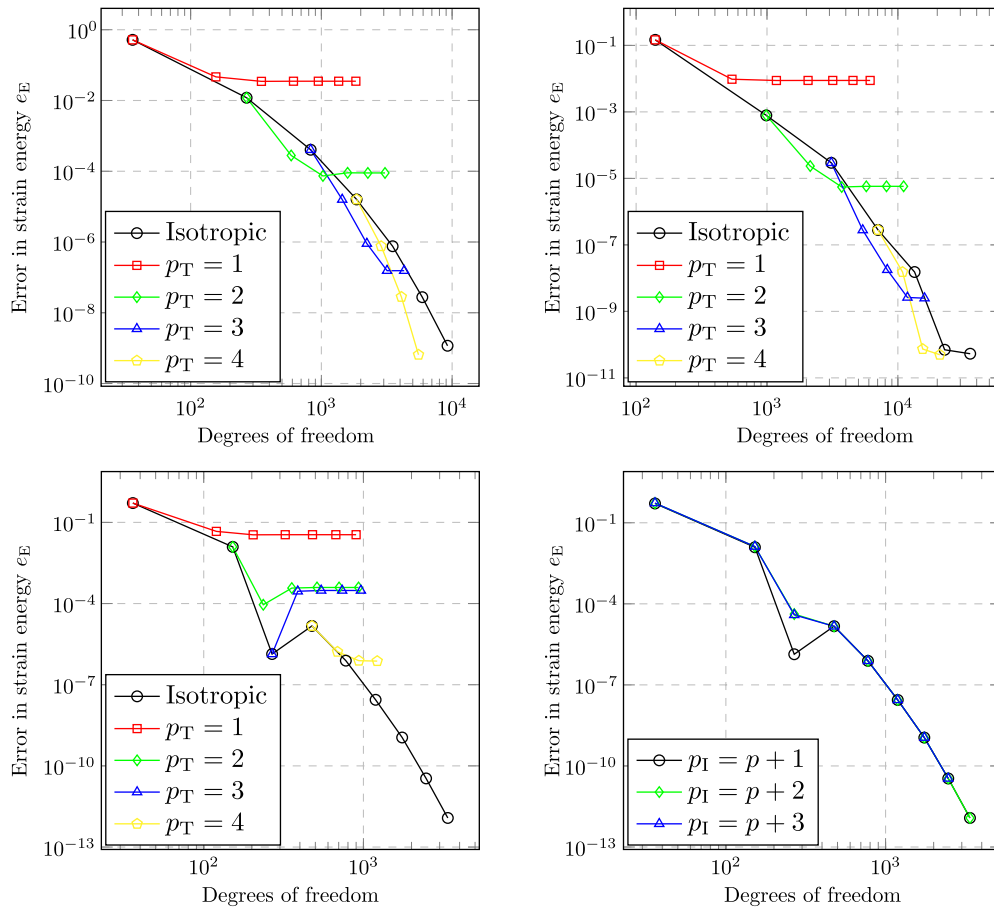


**Fig. 7.** Relative error in strain energy for test case *circular shaped artery*. Top: Results for tensor product space and initial  $(2 \times 4 \times 2)$  mesh (left) and refined  $(4 \times 8 \times 4)$  mesh (right). Bottom: Results for trunk space and initial mesh with standard quadrature (left) and increased order quadrature (right).

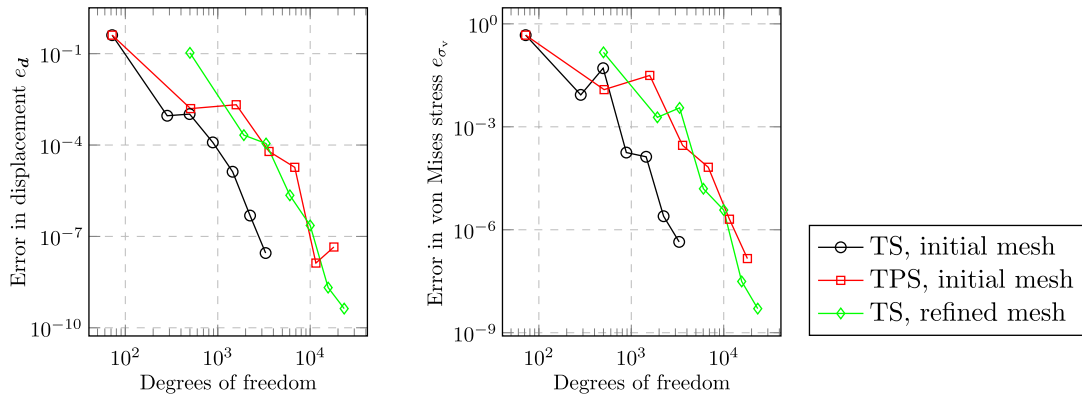


**Fig. 8.** Relative error in displacement and stress for test case *circular shaped artery* with isotropic trunk space (TS) and isotropic tensor product space (TPS).

The left plot shows the flow through the inlet (given as a boundary condition in the fluid subproblem) and the outlet. As a direct consequence of the elasticity of the vessel wall, the flow through the outlet is delayed, the difference between inflow and outflow matches the derivative of the lumen volume with respect to time (Fig. 11 shows an approximation with central differences). Further, Fig. 11 illustrates the procedure applied to obtain a smooth transition from the unloaded state to the state of physiological pressures. For  $t < 1$  s (the first beat of the heart), the inflow and the pressure at the outlet are multiplied by ramp functions to prevent the simulation from becoming unstable due to sudden changes in the pressure and velocity values prescribed at the boundaries. This procedure is explained in more detail in [10]. For  $t \geq 1$  s, all boundary conditions are fully applied such that the system will eventually reach a periodic state. To make sure that any evaluation

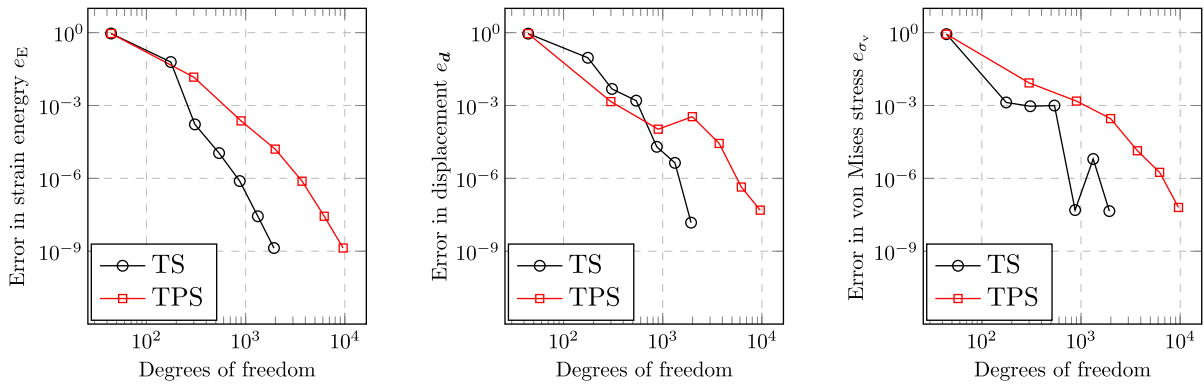


**Fig. 9.** Relative error in strain energy, displacement and stress for test case *idealized bypass graft* with isotropic ansatz spaces and initial mesh.

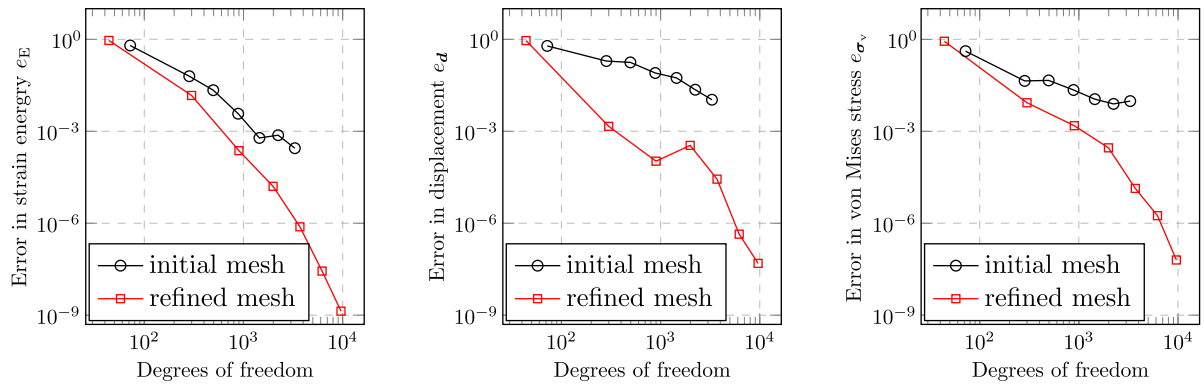


**Fig. 10.** Relative error in strain energy, displacement and stress for test case *irregular shaped artery* with isotropic trunk space.

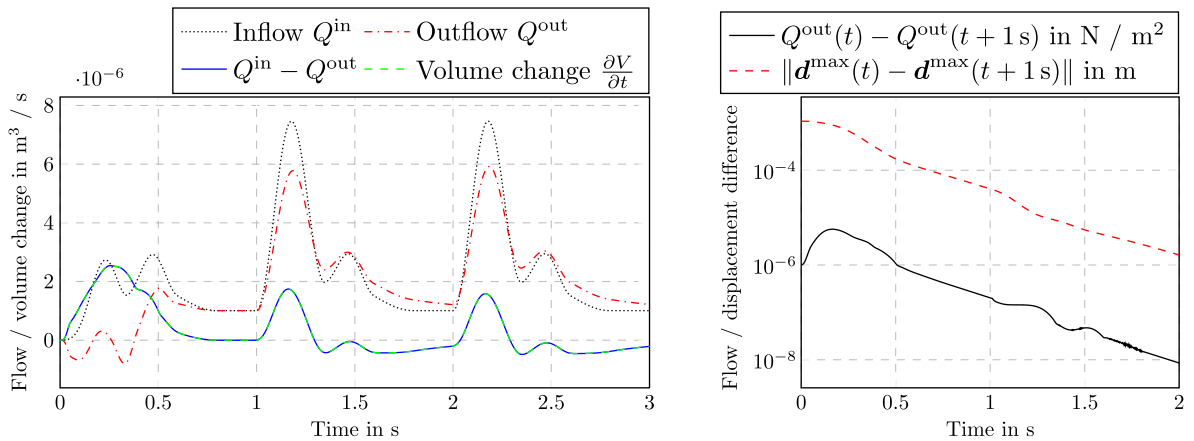


**Fig. 11.** Evolution of the FSI simulations, shown exemplary for variant H-0.5.

is performed for times where this periodic state is reached up to an acceptable tolerance, the right plot in Fig. 11 shows the difference between two successive periods for the outflow as well as for the maximum displacement of the coupling interface. As can be seen, the decay of the difference is close to exponential and we consider the differences at the end of the second period to be small enough. In the following, all quantities are consequently evaluated for  $2\text{ s} < t \leq 3\text{ s}$  if not stated otherwise.

Fig. 12 illustrates the load–displacement relation of the anastomosis. Consistent with observations from clinical practice, the bypass shows a much lower compliance than the artery. Thus, the inner diameters are almost the same at the time instance shown, while the artery's diameter is much smaller in the undeformed state, see Fig. 5.

**Influence of the rigid extension.** As shown in Fig. 5, we consider different extensions, namely a straight (S), a helical (H), and an arc-shaped (A) one which in turn lead to different velocity profiles at the inlet of the actual FSI domain, i.e. the

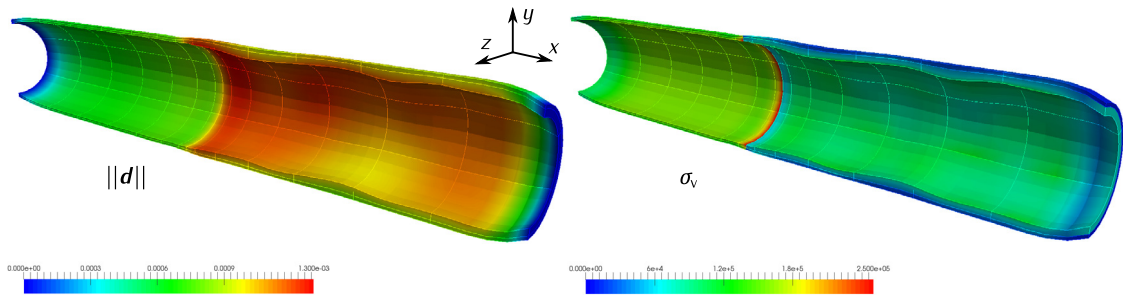


Fig. 12. Displacement (left) and von Mises stress (right) over deformed structural model at time  $t = 2.4$  s.

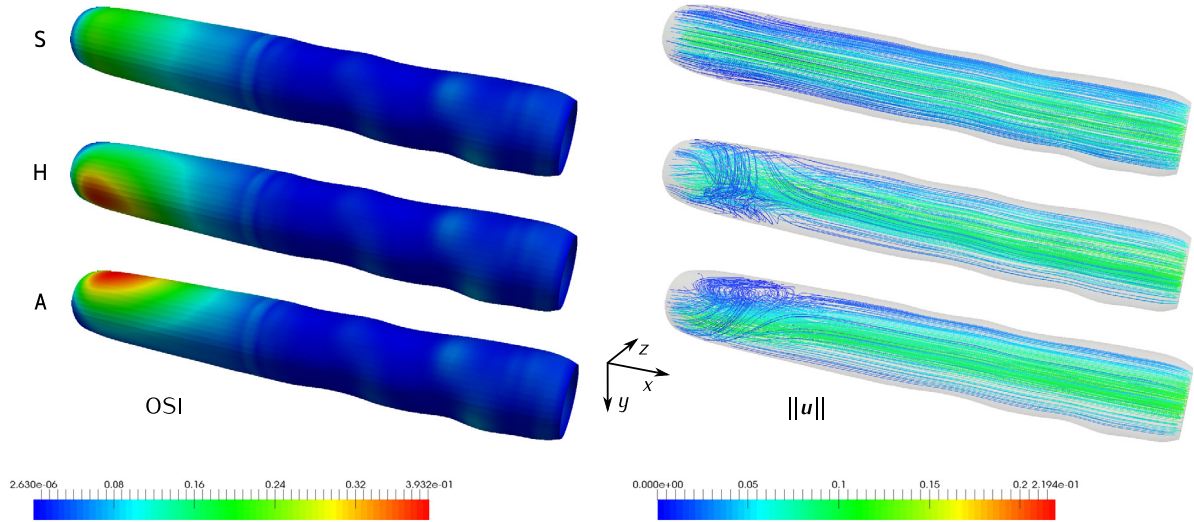
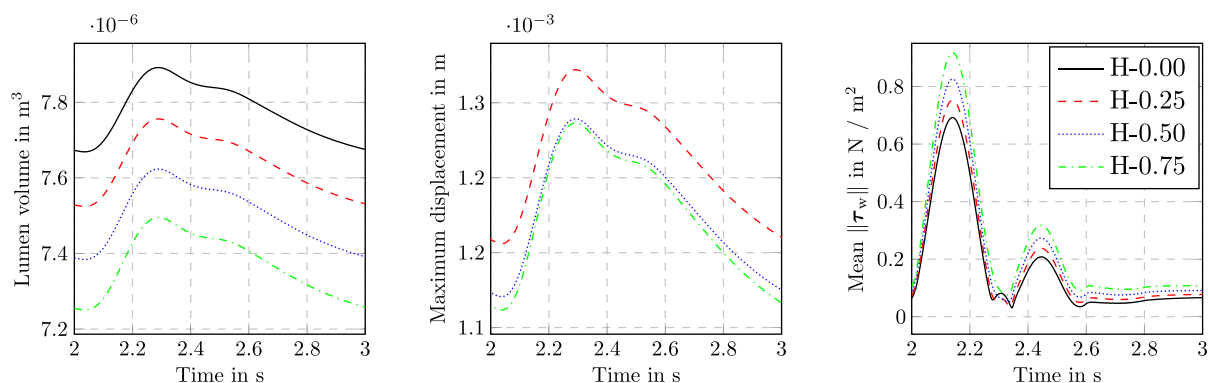


Fig. 13. Oscillating shear index (evaluated for  $2 \text{ s} < t \leq 3 \text{ s}$ ) and streamlines (at  $t = 2.4 \text{ s}$ ) for variants S-0.5, H-0.5 and A-0.5.

inlet of the bypass-graft section. While we are interested in the influence of geometry imperfections in the artery section, considering different inlet velocity profiles provides a reference for the magnitude of variations in the results in general. From the findings in [11] it can be expected that the velocity profile has a much bigger influence on the hemodynamics than the geometry imperfections, especially in the region close to the inlet. However, due to the short length of the vessel considered in [11] it is not clear up to which distance from the inlet this influence is dominant. The present FSI simulations reveal that this distance is actually quite small, and that further downstream, the influence of the geometry imperfections dominate the hemodynamics. The distributions of the OSI and the streamlines shown in Fig. 13 illustrate this. As can be seen, the variations in the OSI are much stronger in the bypass section, which is a direct consequence of the different velocity profiles. Further downstream, in the artery section, the velocity profile has only a negligible influence. As expected according to [11], the variations in the OSI are much smaller, and can be assumed to be directly linked to the geometry imperfections. We will further elaborate this in the next section. Summarizing, it can be said that even though the velocity profile at the inlet of a section has a large influence on the hemodynamics, the influence of geometry imperfections is dominant already at distances of a few (here  $\approx 5$ ) diameters.

*Influence of the geometry imperfections.* We proceed by collecting some exemplary results which are directly influenced by the geometry imperfections. We restrict ourselves on the variant with the helical extension here. If not stated otherwise, the same results were obtained for all extensions as expected according to the above findings. Fig. 14 shows the lumen volume, the maximum displacement of the FSI interface and the mean wall shear stress in the artery section. All quantities seem to be directly linked to the intensity of the geometry imperfection  $d^{\max}$ . Volume and wall shear stress even seem to depend linearly on  $d^{\max}$  while a more general, yet monotonic influence can be observed for the maximum displacement. We assume this to be a result of a change in the location of the maximum displacement as  $d^{\max}$  increases. This will be considered in more detail for the following results.

Fig. 15 shows the maximum WSS for all considered models. The plots also show the corresponding position, i.e. where on the FSI interface the maximum is located. Because for some of the models, the maximum was located very close to the inlet ( $x = 0.03 \text{ m}$ ) or outlet ( $x = 0.06 \text{ m}$ ), only a subsection ( $0.03375 \text{ m} \leq x \leq 0.05625 \text{ m}$ ) of the artery section is considered in Fig. 15. This ensures that the transition from bypass to artery and the clamping of the artery's end do not affect the maximum values. Thus, we can assume that they are only influenced by the geometry imperfections. In contrast



**Fig. 14.** Representative results, which can be directly linked to the intensity of the geometry imperfection  $d^{\max}$ , shown exemplary for the variant with a helical extension.

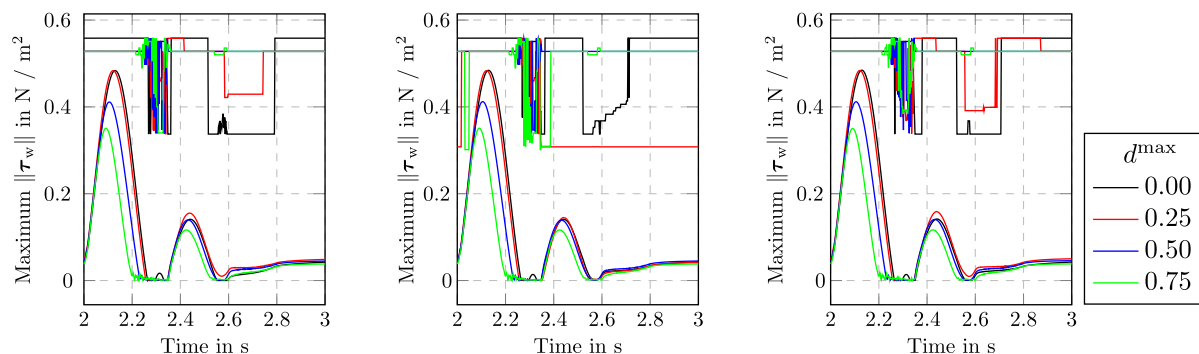


**Fig. 15.** Maximum WSS for variants S, H and A (from left to right) and corresponding location (the x-component of the location multiplied by a factor of  $10 \text{ m}^{-2}$  is shown).

to the quantities shown in Fig. 14, the influence of the intensity of the imperfections  $d^{\max}$  is less intuitive here. Even though the mean WSS increases while increasing  $d^{\max}$ , this does not hold for the maximum WSS. Instead, the lowest maximum WSS is observed for the largest  $d^{\max}$ , showing that the geometry imperfections result in more complicated flows, which cannot be explained by a simple reduction of the mean diameter. While this statement holds regardless of the shape of the extension, Fig. 15 shows that the locations of the maximum WSS are actually not independent of the extension.

A similar observation can be made regarding the stresses inside the vessel wall. Considering again only the mid-part of the artery section ( $0.03375 \text{ m} \leq x \leq 0.05625 \text{ m}$ ) even though the mean wall thickness increases with increasing  $d^{\max}$ , the maximum von Mises stress  $\sigma_v$  is not reduced, but shows an increase, see Fig. 16. The contour plot shown on the right gives rise to the assumption that, like for the maximum WSS in the fluid mechanics subproblem, this is a result of a complex deformation that cannot be explained by a simple increase of the mean wall thickness. Further, the plot on the left shows that dynamic effects may play a role here. As can be seen, at the end of the first period ( $0.5 \text{ s} \lesssim t \lesssim 1 \text{ s}$ ) where the load on the structure remains almost constant, the maximum stress is observed for the smooth model, i.e. the one with the lowest wall thickness. Only for the time intervals characterized by large velocities, the counterintuitive behavior is observed. However, further simulations are needed to clarify such causalities, since the observed phenomena could also be a result of the large displacements at these time intervals or a shift of the contribution to the overall stiffness of the vessel wall towards the media layer.

Finally, we would like to show that the OSI is also directly linked to the intensity of the geometry imperfections. Fig. 17 shows the radius of the lumen as well as the distribution of the OSI for the mid-part of the artery section (again to limit the influence of boundary effects). It should be noted that large values of  $r(x, \varphi)$  are a result of small values of  $d(x, \varphi)$ . While this comparison cannot reveal a one-to-one correspondence, the qualitative similarity between the contours is yet clearly observable. For every dip in the vessel wall, i.e. a region with a locally enlarged radius, the OSI values are also increased. This phenomenon is intensified, wherever the upstream region shows a locally reduced radius. The region of maximum OSI can clearly be identified to be located downstream of the most rapid local increase in diameter, i.e. at a large dip downstream to a large bump in the vessel wall. A quantitative analysis of the relation between the OSI and the intensity of the geometry imperfection is provided in Fig. 18. The right plot shows that regardless of the shape of the rigid extension, the maximum OSI value increases with increasing  $d^{\max}$ . The behavior is similar to that observed for the maximum WSS in Fig. 15. The difference between the smooth model and the one with  $d^{\max} = 0.25 \text{ mm}$  is negligible, while for the models with larger  $d^{\max}$  the differences become larger as well. Looking at the maximum OSI values in the bypass section (Fig. 18 left) the

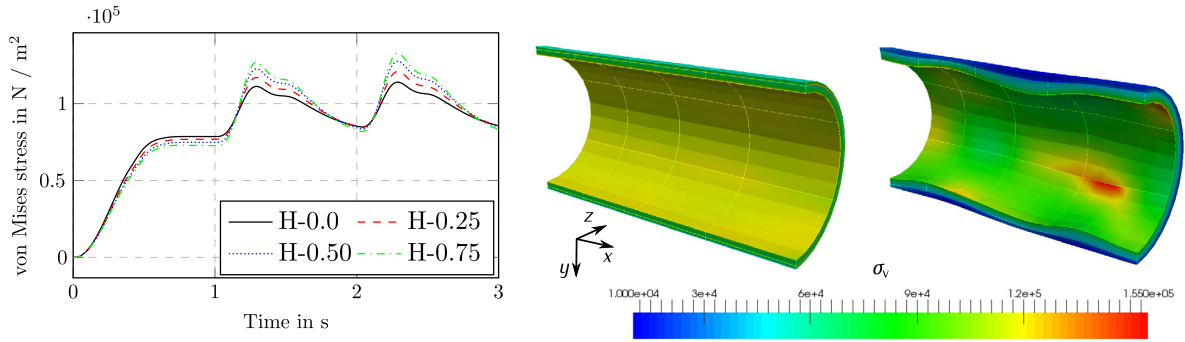


**Fig. 16.** Maximum von Mises Stress for variants with helical extension (left) and stress distribution at  $t = 3.287$  (time of maximum stress) for variant H-0.0 and H-0.75.

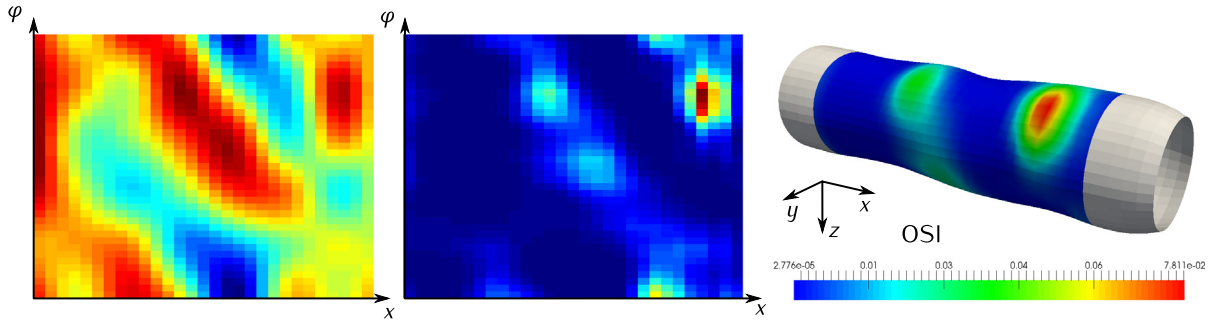


**Fig. 17.** Comparison between radius  $r(x, \varphi)$  (left) and OSI (middle) for variant H-0.5 evaluated for a subsection of the artery segment (right).

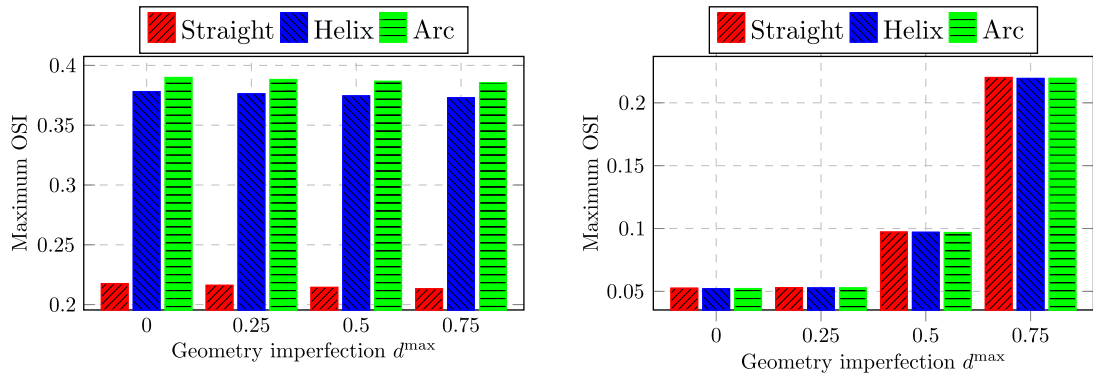


**Fig. 18.** Maximum OSI for bypass section (left), artery section (right).

influence of the rigid extension can also be quantified. The observed OSI values in the range between 0.2 and 0.4 show that the influence of the rigid extension is more severe than that of the geometry imperfections leading to OSI values in the range between 0.005 and 0.025. However, this influence decays rapidly, and, according to the OSI values in the artery section, it is negligible after a distance of a few diameters. Since large curvatures in arteries occur only rarely in the human body, but geometry imperfections occur frequently in diseased vessels, it can be concluded that it is at least as important to model them accurately as it is to prescribe the correct velocity profile at the inlet of the vessel segment under consideration. Of course, different flow rates, blood pressure or material properties may relax this statement which is based on a single choice for all of these parameters so far.

## 5. Conclusion

We presented a study of the FSI in an idealized end-to-end anastomosis between a bypass graft and an artery. The artery's two layers *media* and *adventitia* were modeled using a compressible variant of the HGO material model, while a Neo-Hookean material model was used for the bypass graft. However, the resulting structural model of the anastomosis with its characteristic properties – different stiffness (compliance mismatch), diameter and wall thickness between bypass



graft and artery – only served as a basis for an investigation of influence of geometry imperfections in the artery section on the hemodynamics. An in-depth study of the FSI in anastomoses like this would require a much more sophisticated structural model, including a special treatment of the suture line, for example.

The structural model was discretized using high-order finite elements. To find appropriate polynomial orders and mesh sizes, a convergence study was performed for three different test cases, namely a circular section of an artery, a circular section of a bypass graft and an irregular shaped section of an artery. Up to the authors' knowledge, this study is the first to include an investigation of anisotropic ansatz spaces in combination with soft-tissue material models. Further, a study of the convergence of high-order finite elements for irregular shaped sections of an artery was not performed before. These static simulations reveal a superior performance of the trunk space over the tensor product space, while only for the latter one, a reduction of the ansatz order in thickness direction leads to an improved convergence. Regardless of the ansatz space, a mesh with four elements in the circumferential direction was sufficiently fine for the circular-shaped cases. For the irregular-shaped case, a mesh refinement was necessary to bring the error below an acceptable tolerance.

The FSI problem was solved using a partitioned solution approach, which allows to reuse existing software, specialized for the respective subproblem. Therefore, in combination with the  $p$ -FEM on the structure side, the FVM was employed on the fluid side. A previously designed version of the IQNLS method was successfully used to stabilize and accelerate the coupling iterations despite the large deformations and the little structural damping. For twelve different variants of the FSI model, wall shear stress-related hemodynamic factors were computed. The variants result from a combination of differently intense geometry imperfections and different flow paths of the upstream vessel, leading to different velocity profiles at the inlet of the (straight) vessel section of interest. The simulations reveal a severe influence of the velocity profile close to the inlet, which, however, decays rapidly within a distance of a few diameters from the inlet. At this distance and further downstream, the distributions of wall shear stress and oscillating shear index are only affected by the geometry imperfections. We were able to observe a direct connection between the hemodynamic factors and the shape as well as the intensity of the imperfections. Taking the imperfections to be reductions in radius, the OSI increases in the region downstream of such reductions, such that contours of the vessel radius and the OSI show a qualitatively similar behavior. Similar relations (but not as clear) were also found regarding the WSS and the von Mises stress in the vessel wall. This study therefore promotes the investigation of the underlying FSI phenomena (forming and collapsing of vortices close to the vessel wall) in more detail and shows the importance of incorporating even small geometric imperfections in any model predicting the hemodynamics in blood vessels.

## Acknowledgments

The authors gratefully acknowledge the support provided by the *Forschungszentrum Medizintechnik Hamburg* (fmthh) and by the *Federal Ministry for Economic Affairs and Energy of Germany* (BMWi) in the scope of the joint project HyStOH (project number 03SX409C).

## References

- [1] M. Anliker, R. Rockwell, E. Ogden, Nonlinear analysis of flow pulses and shock waves in arteries, *Z. Angew. Math. Phys.* 22 (2) (1971) 217–246.
- [2] T.J. Hughes, J. Lubliner, On the one-dimensional theory of blood flow in the larger vessels, *Math. Biosci.* 18 (1–2) (1973) 161–170. [http://dx.doi.org/10.1016/0025-5564\(73\)90027-8](http://dx.doi.org/10.1016/0025-5564(73)90027-8).
- [3] C. Figueroa, I. Vignon-Clementel, K. Jansen, T. Hughes, C.A. Taylor, A coupled momentum method for modeling blood flow in three-dimensional deformable arteries, *Comput. Methods Appl. Mech. Engrg.* 195 (41–43) (2006) 5685–5706.
- [4] Y. Bazilevs, M.-C. Hsu, Y. Zhang, W. Wang, T. Kvamsdal, S. Hentschel, J. Isaksen, Computational vascular fluid–structure interaction: methodology and application to cerebral aneurysms, *Biomech. Model. Mechanobiol.* 9 (4) (2010) 481–498. <http://dx.doi.org/10.1007/s10237-010-0189-7>.
- [5] J.G. Isaksen, Y. Bazilevs, T. Kvamsdal, Y. Zhang, J.H. Kaspersen, K. Waterloo, B. Romner, T. Ingebrigtsen, Determination of wall tension in cerebral artery aneurysms by numerical simulation, *Stroke* 39 (12) (2008) 3172–3178. <http://dx.doi.org/10.1161/STROKEAHA.107.503698>.
- [6] R. Torii, M. Oshima, T. Kobayashi, K. Takagi, T.E. Tezduyar, Fluid–structure interaction modeling of a patient-specific cerebral aneurysm: influence of structural modeling, *Comput. Mech.* 43 (1) (2008) 151–159. <http://dx.doi.org/10.1007/s00466-008-0325-8>.
- [7] M. Alishahi, M.M. Alishahi, H. Emdad, Numerical simulation of blood flow in a flexible stenosed abdominal real aorta, *Sci. Iran.* 18 (6) (2011) 1297–1305. <http://dx.doi.org/10.1016/j.scient.2011.11.021>.
- [8] H. Suito, K. Takizawa, V.Q.H. Huynh, D. Sze, T. Ueda, FSI analysis of the blood flow and geometrical characteristics in the thoracic aorta, *Comput. Mech.* 54 (4) (2014) 1035–1045. <http://dx.doi.org/10.1007/s00466-014-1017-1>.
- [9] V. Peiffer, S.J. Sherwin, P.D. Weinberg, Does low and oscillatory wall shear stress correlate spatially with early atherosclerosis? A systematic review, *Cardiovasc. Res.* 99 (2) (2013) 242–250. <http://dx.doi.org/10.1093/cvr/cvt044>.
- [10] L. Radtke, A. Larena-Avellaneda, E. Debus, A. Düster, Convergence acceleration for partitioned simulations of the fluid–structure interaction in arteries, *Comput. Mech.* 57 (6) (2016) 901–920. <http://dx.doi.org/10.1007/s00466-016-1268-0>.
- [11] L. Radtke, A. Larena-Avellaneda, T. Kölbl, E. Debus, A. Düster, Cardiovascular fluid–structure interaction: A partitioned approach utilizing the  $p$ -FEM, *Proc. Appl. Math. Mech.* 14 (2014) 493–494. <http://dx.doi.org/10.1002/pamm.201410234>.
- [12] H. Bungartz, M. Schäfer (Eds.), Fluid–Structure Interaction, Modelling, Simulation and Optimisation, in: *Lecture Notes in Computational Science and Engineering*, vol. 53, Springer, 2006.
- [13] H. Bungartz, M. Mehl, M. Schäfer (Eds.), Fluid–Structure Interaction II, Modelling, Simulation, Optimisation, in: *Lecture Notes in Computational Science and Engineering*, vol. 73, Springer, 2010.
- [14] Y. Bazilevs, K. Takizawa, T. Tezduyar, Computational Fluid–Structure Interaction: Methods and Applications, in: *Wiley Series in Computational Mechanics*, John Wiley & Sons, 2013.
- [15] R. Torii, M. Oshima, T. Kobayashi, K. Takagi, T.E. Tezduyar, Computer modeling of cardiovascular fluid–structure interactions with the deforming-spatial-domain/stabilized space–time formulation, *Comput. Methods Appl. Mech. Engrg.* 195 (13–16) (2006) 1885–1895. <http://dx.doi.org/10.1016/j.cma.2005.05.050>.



- [16] R. Torii, M. Oshima, T. Kobayashi, K. Takagi, T.E. Tezduyar, Influence of wall elasticity in patient-specific hemodynamic simulations, *Comput. & Fluids* 36 (1) (2007) 160–168.
- [17] T.E. Tezduyar, S. Sathe, T. Cragin, B. Nanna, B.S. Conklin, J. Pausewang, M. Schwaab, Modelling of fluid–structure interactions with the space–time finite elements: Arterial fluid mechanics, *Internat. J. Numer. Methods Fluids* 54 (6–8) (2007) 901–922.
- [18] T.E. Tezduyar, S. Sathe, M. Schwaab, B.S. Conklin, Arterial fluid mechanics modeling with the stabilized space–time fluid–structure interaction technique, *Internat. J. Numer. Methods Fluids* 57 (5) (2008) 601–629. <http://dx.doi.org/10.1002/fld.1633>.
- [19] Y. Bazilevs, M.-C. Hsu, D. Benson, S. Sankaran, A. Marsden, Computational fluid–structure interaction: methods and application to a total cavopulmonary connection, *Physiol. Rev.* 45 (2009) 77–89.
- [20] K. Takizawa, C. Moorman, S. Wright, J. Christopher, T.E. Tezduyar, Wall shear stress calculations in space–time finite element computation of arterial fluid–structure interactions, *Comput. Mech.* 46 (1) (2010) 31–41. <http://dx.doi.org/10.1007/s00466-009-0425-0>.
- [21] K. Takizawa, Y. Bazilevs, T.E. Tezduyar, C.C. Long, A.L. Marsden, K. Schjodt, Patient-Specific Cardiovascular Fluid Mechanics Analysis with the ST and ALE-VMS Methods, in: S.R. Idelsohn (Ed.), *Numerical Simulations of Coupled Problems in Engineering*, in: *Computational Methods in Applied Sciences*, vol. 33, Springer International Publishing, 2014, pp. 71–102. [http://dx.doi.org/10.1007/978-3-319-06136-8\\_4](http://dx.doi.org/10.1007/978-3-319-06136-8_4).
- [22] F. Kabinejadian, D.N. Ghista, Compliant model of a coupled sequential coronary arterial bypass graft: Effects of vessel wall elasticity and non-Newtonian rheology on blood flow regime and hemodynamic parameters distribution, *Med. Eng. Phys.* 34 (7) (2012) 860–872.
- [23] R. Torii, N.B. Wood, N. Hadjiloizou, A.W. Dowsey, A.R. Wright, A.D. Hughes, J. Davies, D.P. Francis, J. Mayet, G.-Z. Yang, S.A.M. Thom, X.Y. Xu, Fluid–structure interaction analysis of a patient-specific right coronary artery with physiological velocity and pressure waveforms, *Comm. Numer. Methods Engrg.* 25 (5) (2009) 565–580. <http://dx.doi.org/10.1002/cnm.1231>.
- [24] U. Küttler, M. Gee, C. Förster, A. Comerford, W.A. Wall, Coupling strategies for biomedical fluid–structure interaction problems, *Int. J. Numer. Methods Biomed. Eng.* 26 (3–4) (2010) 305–321. <http://dx.doi.org/10.1002/cnm.1281>.
- [25] J. Degroote, K.-J. Bathe, J. Vierendeels, Performance of a new partitioned procedure versus a monolithic procedure in fluid–structure interaction, *Comput. Struct.* 87 (2009) 793–801.
- [26] J. Degroote, R. Haelterman, S. Annerel, P. Bruggeman, J. Vierendeels, Performance of partitioned procedures in fluid–structure interaction, *Comput. Struct.* 88 (7–8) (2010) 446–457.
- [27] J. Degroote, J. Vierendeels, Multi-solver algorithms for the partitioned simulation of fluid–structure interaction, *Comput. Methods Appl. Mech. Engrg.* 200 (25–28) (2011) 2195–2210.
- [28] P. Erbts, S. Hartmann, A. Düster, A partitioned solution approach for electro-thermo-mechanical problems, *Arch. Appl. Mech.* 85 (2015) 1075–1101. <http://dx.doi.org/10.1007/s00419-014-0941-z>.
- [29] G. Wendt, P. Erbts, A. Düster, Partitioned coupling strategies for multi-physically coupled radiative heat transfer problems, *J. Comput. Phys.* 300 (2015) 327–351. <http://dx.doi.org/10.1016/j.jcp.2015.07.063>.
- [30] G. Holzapfel, T. Gasser, R. Ogden, A new constitutive framework for arterial wall mechanics and a comparative study of material models, *J. Elast. Phys. Sci. Solids* 61 (1–3) (2000) 1–48.
- [31] Z. Yosibash, E. Priel, Artery active mechanical response: High order finite element implementation and investigation, *Comput. Methods Appl. Mech. Engrg.* 237–240 (0) (2012) 51–66.
- [32] Z. Yosibash, E. Priel, p-fems for hyperelastic anisotropic nearly incompressible materials under finite deformations with applications to arteries simulation, *Internat. J. Numer. Methods Engrg.* 88 (11) (2011) 1152–1174. <http://dx.doi.org/10.1002/nme.3213>.
- [33] D. Nolan, A. Gower, M. Destrade, R. Ogden, J. McGarry, A robust anisotropic hyperelastic formulation for the modelling of soft tissue, *J. Mech. Behav. Biomed. Mater.* 39 (2014) 48–60.
- [34] B. Szabó, I. Babuška, *Finite Element Analysis*, John Wiley & Sons, 1991.
- [35] M. König, L. Radtke, A. Düster, A flexible C++ framework for the partitioned solution of strongly coupled multifield problems, *Comput. Math. Appl.* 72 (2016) 1764–1789. <http://dx.doi.org/10.1016/j.camwa.2016.07.031>.
- [36] P. Wriggers, *Nonlinear Finite-Element-Methods*, Springer-Verlag, 2009.
- [37] J. Bonet, R. Wood, *Nonlinear Continuum Mechanics for Finite Element Analysis*, Cambridge University Press, New York, 1997.
- [38] O. Zienkiewicz, R. Taylor, *The Finite Element Method – Solid Mechanics*, Vol. 2, fifth ed., Butterworth-Heinemann, 2000.
- [39] G. Holzapfel, *Nonlinear Solid Mechanics*, John Wiley & Sons, 2000.
- [40] K. Takizawa, H. Takagi, T.E. Tezduyar, R. Torii, Estimation of element-based zero-stress state for arterial FSI computations, *Comput. Mech.* 54 (4) (2014) 895–910. <http://dx.doi.org/10.1007/s00466-013-0919-7>.
- [41] S. Hartmann, *Finite-Elemente Berechnung inelastischer Kontinua – Interpretation als Algebroid-Differentialgleichungssysteme* (Postdoctoral thesis), Institut für Mechanik, Universität Kassel, 2003.
- [42] K. Takizawa, J. Christopher, T.E. Tezduyar, S. Sathe, Space–time finite element computation of arterial fluid–structure interactions with patient-specific data, *Int. J. Numer. Methods Biomed. Eng.* 26 (1) (2010) 101–116.
- [43] J. Ferziger, M. Peric, *Computational Methods for Fluid Dynamics*, third ed., Springer-Verlag, Berlin, Heidelberg, 2002.
- [44] O. Zienkiewicz, R. Taylor, *The Finite Element Method – Fluid Dynamics*, Vol. 3, fifth ed., Butterworth-Heinemann, 2000.
- [45] J. Reddy, D.K. Gartling, *The Finite Element Method in Heat Transfer and Fluid Dynamics*, third ed., CRC Press, Taylor & Francis Group, 2010.
- [46] <http://www.openfoam.org>.
- [47] H. Jasak, A. Jemcov, Z. Tukovic, OpenFOAM: A C++ Library for Complex Physics Simulations, in: *Proceedings of the International Workshop on Coupled Methods in Numerical Dynamics / Terze, Zdravko, Dubrovnik, Hrvatska, 2007*, pp. 47–66.
- [48] H. Jasak, Dynamic Mesh Handling in OpenFOAM, in: *47th AIAA Aerospace Sciences Meeting including The New Horizons Forum and Aerospace Exposition / Orlando, Florida, Orlando, Florida, 2009*, pp. 1–10. <http://dx.doi.org/10.2514/6.2009-341>.
- [49] I. Babuška, B.A. Szabo, I.N. Katz, The p-version of the finite element method, *SIAM J. Numer. Anal.* 18 (1981) 515–545.
- [50] M. Suri, I. Babuška, C. Schwab, Locking effects in the finite element approximation of plate models, *Math. Comp.* 64 (1995) 461–482.
- [51] M. Suri, Analytical and computational assessment of locking in the hp finite element method, *Comput. Methods Appl. Mech. Engrg.* 133 (1996) 347–371.
- [52] U. Heißer, S. Hartmann, A. Düster, Z. Yosibash, On volumetric locking-free behavior of p-version finite elements under finite deformations, *Comm. Numer. Methods Engrg.* 24 (11) (2008) 1019–1032.
- [53] J.A. Cottrell, T.J.R. Hughes, Y. Bazilevs, *Isogeometric Analysis: Towards Integration of CAD and FEM*, John Wiley & Sons, 2009.
- [54] G. Királyfalvi, B. Szabó, Quasi-regional mapping for the p-version of the finite element method, *Finite Elem. Anal. Des.* 27 (1997) 85–97.
- [55] A. Düster, H. Bröker, E. Rank, The p-version of the finite element method for three-dimensional curved thin walled structures, *Internat. J. Numer. Methods Engrg.* 52 (2001) 673–703.
- [56] B. Szabó, A. Düster, E. Rank, The p-version of the finite element method, in: E. Stein, R. de Borst, T.J.R. Hughes (Eds.), *Encyclopedia of Computational Mechanics*, Vol. 1, John Wiley & Sons, 2004, pp. 119–139. <http://dx.doi.org/10.1002/0470091355.ecm003g> (Chapter 5).
- [57] T. Gasser, C. Schulze-Bauer, G.A. Holzapfel, A three-dimensional finite element model for arterial clamping, *J. Biomech. Eng.* 124 (4) (2002) 255–363.
- [58] C. Körner, *Die Silikon-beschichtete Polyesterprothese: Konzept, physikalische und biologische Eigenschaften* (Dissertation), Bayerische Julius-Maximilians-Universität Würzburg, 2007.